atmosphere

MDPI

Article

WRF-LES Simulation of the Boundary Layer Turbulent Processes during the BLLAST Campaign

Mireia Udina [1,*], Àlex Montornès [2], Pau Casso [2], Branko Kosović [3] and Joan Bech [1]

[1] Departament de Física Aplicada-Meteorologia, Universitat de Barcelona, C/ Martí i Franquès, 1, 08028 Barcelona, Spain; joan.bech@ub.edu
[2] VORTEX, 08042 Barcelona, Spain; alex.montornes@vortex.es (À.M.); pau.casso@vortex.es (P.C.)
[3] National Center for Atmospheric Research, Boulder, CO 80307, USA; branko@ucar.edu
* Correspondence: mudina@meteo.ub.edu

Received: 8 September 2020; Accepted: 19 October 2020; Published: 24 October 2020

Abstract: A real case long-term nested large eddy simulation (LES) of 25-day duration is performed using the WRF-LES modelling system, with a maximum horizontal grid resolution of 111 m, in order to explore the ability of the model to reproduce the turbulence magnitudes within the first tens of metres of the boundary layer. Sonic anemometer measurements from a 60-m tower installed during the Boundary Layer Late Afternoon and Sunset Turbulence (BLLAST) field campaign are used for verification, which is focused on the turbulent magnitudes in order to assess the success and limitations in resolving turbulent flow characteristics. The mesoscale and LES simulations reproduce the wind speed and direction fairly well, but only LES is able to reproduce the energy of eddies with lifetimes shorter than a few hours. The turbulent kinetic energy in LES simulation is generally underestimated during the daytime, mainly due to a vertical velocity standard deviation that is too low. The turbulent heat flux is misrepresented in the model, probably due to the inaccuracy of the sub-grid scheme.

Keywords: large eddy simulation; verification; turbulence; WRF

1. Introduction

A good representation of the atmospheric flow field over complex and non-homogeneous terrain requires numerical modelling using spatial resolution of the order of hectometres or less, broadly referred as large eddy simulation (LES), to include the land use and terrain modifications on the atmospheric boundary layer (ABL) flow field. Moreover, in order to obtain a complete representation of the physical processes involved, a different range of scales needs to be resolved, from small motion scales to mesoscale and synoptic scales. Dynamical downscaling including multi-scale simulations down to LES domains which include resolved turbulence interactions is still an ongoing research topic.

In the Weather Research and Forecasting (WRF) model, turbulent stresses and fluxes are usually modelled using 1D PBL parameterisations, which assume horizontal homogeneity, an approximation that can be done if the grid size is relatively large (e.g., few kilometres to tens of kilometres). In this approach, the equations of the flow field are resolved using the Reynolds-averaged Navier–Stokes (RANS) technique where turbulent motions are fully parametrised [1]. Instead, if the horizontal cell grid size decreases to a few km or tens or hundreds of metres, the assumption of horizontal homogeneity is not valid and the effect of horizontal gradients of turbulent stresses and fluxes should be included [2]. Turbulence is explicitly resolved using the large eddy simulation (LES) approximation, where the large eddies are resolved and the small eddies are modelled in a sub-grid scheme. The cross-scale coupling system WRF-LES [3] allows the simulation of the flow field in a wide range of scale processes, from mesoscale to microscale, being able to resolve the mean quantities and

turbulent stresses and fluxes. However, it is known that in the coupling model domain configuration, there will always be a range of grid resolutions where certain processes are neither sub-grid nor resolved, the so-called "grey zone" or "terra incognita" [4]. As recently suggested by [5–7], comparison and intercomparison projects of real long simulation time periods are needed in order to establish the progresses in the cross-scale simulations and identify the necessities for the future modelling strategies.

During the last decades, researchers have used LES approximation to study specific problems such as air pollution dispersion in urban street canyons [8–10], flow distortion caused by wind turbines [11–13], large fires [14,15] or cloud and precipitation processes development [16–19]. Many other studies have used real case LES to simulate atmospheric flows in complex terrain areas [20–22] where grid sizes of few hundreds of metres are needed to resolve the terrain elevation and LES approximation is required. Other authors suggested the need to use LES to resolve small-scale turbulent processes in complex terrain such as downslope windstorms [23], low-level turbulence and rotors [24,25], precipitation dynamics [26–29] or other small scale processes. Recently, the authors of [30,31] used WRF-LES with domains nested within mesoscale domains and examined the resulting flow field. However, none of them regarded the turbulent quantities, nor explored the ability of the simulation to reproduce the fluxes, variances and turbulence intensity. In addition, a number of previous LES studies are conceived as idealised theoretical studies (e.g., [32–35]), allowing to isolate specific atmospheric phenomena, while others are designed as real case studies, which need to be compared with proper high-resolution observational data sets. Some recent case studies consider simulation periods of one or few days (e.g., [22,36,37]) which allows sensitivity tests varying the model configuration but restricts the verification process and hampers the evaluation of the general quality of the simulations. In this paper, we report a large eddy simulation using the WRF-LES system spanning 25 days during a field experimental campaign.

In order to explore the accuracy of WRF-LES simulations in reproducing turbulent quantities, we use realistic LES simulations of 111-m horizontal grid size here and we compare the results with the observational data set from the Boundary-Layer Late Afternoon and Sunset Turbulence (BLLAST) campaign [38], which took place during early summer 2011 in France, north of the central French Pyrenean foothills. Therefore, the objective of this paper is to compare a long-term (25-day) real case WRF-LES simulation with observations including mean and turbulent quantities in the first tens of metres above ground, exploring the ability of the model to reproduce the magnitude, time evolution and associated energy of the atmospheric flow field.

The structure of the rest of the paper is as follows. The area of study, observations and model simulations configuration are described in Section 2 together with the methodology used to carry out the comparison. Results and discussion are given in Section 3, evaluating the mean and turbulent quantities. Finally, in Section 4 conclusions are formulated along with final remarks.

2. Site, Data and Methods

2.1. Site and Tower Measurements

The BLLAST site is located on the Plateau de Lannemezan, north of the central French Pyrenean foothills. Locally, it is a relatively flat terrain area but it is influenced by complex terrain features, mountains and valleys in its surroundings. In particular, the site is about 11 km north of the base of the first range of the Pyrenees mountain massif with peaks of around 1500 to 2000 m a.s.l. and is about 40 km far from the highest peaks of the mountain range, exceeding 3000 m a.s.l. (Figure 1). The Pyrenees mountains have a large influence on atmospheric flows of the region both at mesoscale and synoptic scale, as highlighted in a number of numerical meteorological case studies-see for example [39–42].

A 60 m tower called Valimev Tower was placed at the surface-site 4 (ss4) in Site 1 defined in the BLLAST campaign [38] at 43.1242° N, 0.3625° E (Figure 1). The Valimev Tower sensors were located at 29.4 m, 45.8 m and 61.4 m (named hereafter z_{30}, z_{45} and z_{60}, respectively), equipped by 3D sonic

anemometers (Table 1), which are able to measure the three wind components, u, v and w and the temperature at 10 Hz frequency. The data set for this tower starts on 14 June 2011 for the z_{30} and z_{45} levels, and slightly later for the z_{60} level, between 10:00 and 11:00 UTC on 15 June 2011, and finishes on 8 July 2011 for the three levels. The calculated standard deviations of the three wind components and the averaged heat flux with a 5 min temporal averaging are used. We applied the corrections and filters indicated in [43]. Additionally, sonic measurements were not considered during rainfall periods or when σ_u, σ_v or σ_w were greater than 2 m s^{-1}, mostly before or after rainfall periods. In summary, the sonic anemometer measurements obtained from the Valimev Tower during the BLLAST campaign enables to evaluate the model simulations during 25 days (24 days for z_{60}).

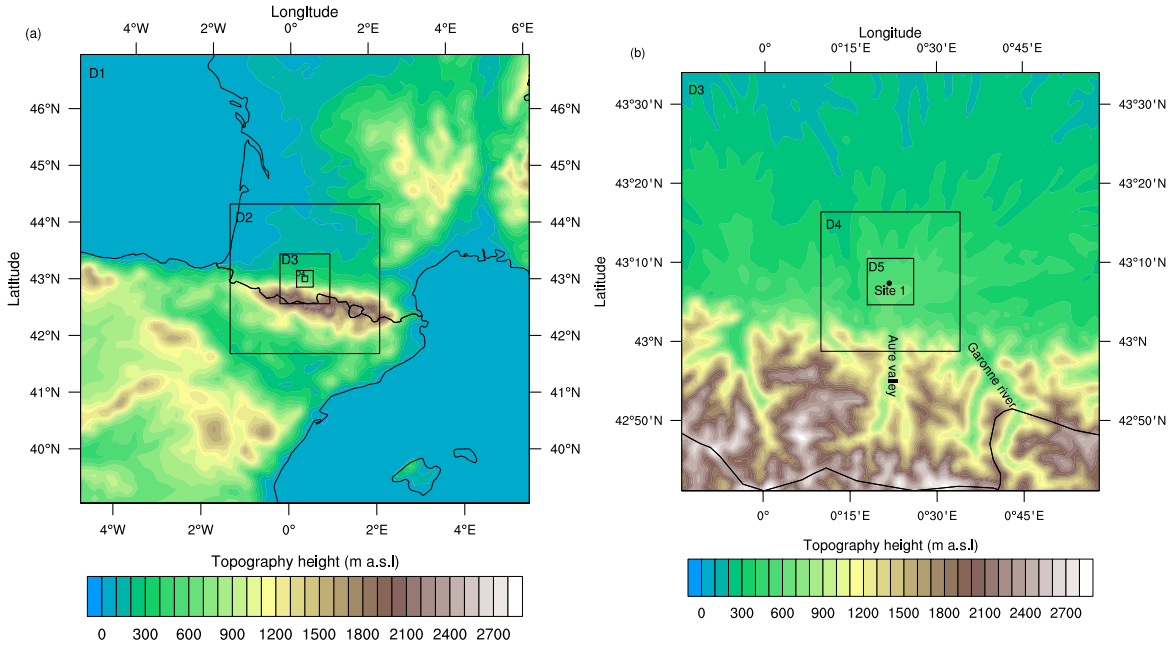

Figure 1. (**a**) Topography of domain D1 including north of Spain and south of France, with the modelling nested domains. (**b**) Topography, domains D3, D4 and D5 and location of site 1.

Table 1. Tower levels, sensors and data period.

Level Name	Height (m)	Sensors	Data Period
z_{30}	29.4	Campbell Csat3 3D sonic anemometer	14 June 2011–8 July 2011
z_{45}	45.8	Gill master pro 3D sonic anemometer, wind vane	
z_{60}	61.4	Campbell Csat3 3D sonic anemometer	15 June 2011–8 July 2011

2.2. WRF-LES Simulations

A long-term simulation is run with the WRF model version 3.6.1 [44] following a configuration previously developed and tested at 85 sites all over the world for wind resource application [45]. Five nested domains centred at Site 1 (see Section 2.1) are configured. The outermost and innermost domains have a horizontal resolutions of 9 km (D1) and 111 m (D5), respectively. The relationship between domains is a ratio of 1:3 as generally used. Simulation is divided in two parts. First, a mesoscale run from 9 to 1 km with two-way nesting feedback enabled. This part is run employing so-called "mesoscale mode" (MESO), which means applying the most-commonly used Reynolds-averaged Navier-Stokes (RANS) decomposition. Second, a microscale run from 333 m to 111 m by using the mesoscale output as initial and lateral boundary conditions (LBC). These simulations are performed in "microscale mode" using the LES approach instead of a PBL scheme (see Table 2). A two dimensional Smagorinsky closure is applied in MESO domains [46]. For LES domains a three-dimensional LES turbulence closure is used as a sub-grid scheme, including a

prognostic equation for TKE [46,47]. One challenge in meso-micro scale coupling is the non-turbulent state of LBCs. In order to fix this issue, the perturbation potential method of LBC is applied [48,49]. The model top is set at 50 hPa, and a 5 km damping layer is included in order to prevent wave reflection. A fixed number of vertical levels (38) are used in all domains, with the first level located at around 8 m above ground level and 15 levels included in the first 1000 m of the atmosphere. Although several papers using WRF-LES in recent literature settle a greater number of vertical levels (e.g., [6,22,35,37]), our choice of 15 levels within the first km is a compromise choice between between computational cost and simulation performance for the long-term period of 25 days. Simulation tests increasing vertical levels (from 15 to 22 vertical levels in the first km of atmosphere) for a 4-day simulated period (1–4 July 2011) did not reveal much better results (see Appendix A).

The WRF physics package used here includes the rapid radiative transfer model (RRTM) for longwave radiation [50], the Dudhia parametrisation for shortwave radiation [51] and the Noah land-surface parametrisation [52]. Domains D1, D2 and D3 use the revised MM5 surface layer parametrization [53] and the Mellor–Yamada–Janjić (MYJ) model [54] for boundary-layer parametrisation, a widely used local scheme that has a prognostic equation for the TKE. Cumulus are not parameterised in these domains. Domains D4 and D5 use WRF Single-Moment 3-class scheme microphysics parametrisation [55] and the Monin-Obukhov similarity theory for surface layer parameterisation [56]. Static data of topography elevation and land use are adapted from global databases to the WRF preprocessing system (WPS). The Shuttle Radar Topography Mission (SRTM) [57] with 3 arc-seconds resolution (∼90 m) global coverage is used for the topography and the the GlobCover [58] for land use database.

The simulated period spans for 25 days, from 14 June 2011 to 8 July 2011, when the BLLAST campaign took place. The initial and boundary conditions are given by ERA5 [59] with horizontal resolution of 30 km, 38 vertical levels and temporal resolution of 1 h. For this study, mesoscale and microscale outputs at 1 km and 111 m are considered. Mesoscale and microscale outputs have a different postprocessing. In the first case, WRF output is set to 10 min. In the microscale case, outputs are saved every 0.25 s and a 10-min average and standard deviation for the main fields are computed later.

Table 2. WRF model set-up. The number of grid points in x, y and z is marked with nx, ny, nz.

Domain	nx × ny × nz	Grid	Mode	PBL Scheme
D1		9 km	RANS	MYJ
D2		3 km	RANS	MYJ
D3	99 × 99 × 38	1 km	RANS	MYJ
D4		333 m	LES	-
D5		111 m	LES	-

2.3. Quantities and Statistics

Mean and turbulent quantities are evaluated at three levels of the tower, z_{30}, z_{45} and z_{60}. The evaluated mean quantities include the horizontal wind speed and wind direction. On the contrary, mean temperature from the sonic anemometers are not considered, as this variable can be underestimated due to the CSAT firmware, because the speed of sound is also underestimated, specially in high winds [60]. The verified turbulent quantities are the standard deviations of the three wind components (σ_u, σ_v and σ_w), gathered with the turbulent kinetic energy (TKE) calculated as $TKE = 0.5(\sigma_u^2 + \sigma_v^2 + \sigma_w^2)$ and the heat flux (F_H) expressed as $F_H = \overline{w'T'}$.

The model verification has been performed at 10 min time steps, a temporal resolution deemed appropriate for this type of study. Three verification scores have been considered, namely the mean

bias (MB) (Equation (1)), root mean square error (RMSE) (Equation (2)) and regression coefficient (R) (Equation (3)), given by:

$$MB = \frac{1}{n}\sum_{i=1}^{n} m_i - o_i \tag{1}$$

$$RMSE = \sqrt{\frac{1}{n}\sum_{i=1}^{n}(m_i - o_i)^2} \tag{2}$$

$$R = \frac{\sum_{i=1}^{n}(m_i - \overline{m})(o_i - \overline{o})}{\sum_{i=1}^{n}(m_i - \overline{m})^2} \tag{3}$$

where m_i and o_i are, respectively, the model and the observation values at time step i and n is the total number of time steps.

Contingency tables were used to evaluate the horizontal wind speed according to the following verification scores: threat score (TS), probability of detection (POD) and false alarm ratio (FAR)-see Appendix B.

3. Results and Discussion

The results presented herein are divided in two sections. Firstly, the model verification of the mean quantities is explored, stratifying results by height levels. Secondly, the turbulent quantities are evaluated, regarding their temporal evolution, data distributions, daily cycle representations and turbulence spectrum description.

3.1. Model Performance: Mean Quantities

Figure 2 shows the distribution of horizontal wind speed and wind direction through wind roses at three different heights, given by the tower observations (OBS), the mesoscale simulation of 1-km horizontal grid (MESO) and the LES simulation of 111-m horizontal grid (LES). Horizontal wind speed below 0.5 m s^{-1} are considered as calm winds and not plotted, as the wind direction cannot be determined reliably at these speeds. The dominant wind component from measurements is NW, which is also reproduced in the simulations, increasingly as the height above ground increases. According to previous studies from BLLAST campaign (e.g., [61,62]), northern and western components are mostly associated with large scale circulation, such as frontal passages and strong synoptic flows. The observed light winds from the N and NE directions corresponding to daytime mountain breezes [63] are misrepresented in the MESO and LES simulations. Instead, the S and SE nocturnal flows are well captured by the LES simulation, although simulations tend to exaggerate the frequency of SE flows, specially LES, and to shift slightly the wind towards the east.

In Figure 3 time series of horizontal wind speed and direction observations at z_{30} are compared with MESO and LES simulations. Model simulations are able to reproduce the wind speed evolution tendencies (Figure 3a), slightly overestimating the values, as indicated by the Mean Bias (MB) which is positive in all levels and simulations (Table 3). Simulations show relatively low values of RMSE, between 1.25 and 1.52 m s^{-1} on the three levels (see Table 3), meaning that the wind speed values are relatively well estimated. The linear regression coefficient (R) ranges between 0.45 and 0.66 in different simulations and levels, and is slightly better for MESO than for LES simulations. Moreover the linear regression improves as the height above ground increases, so that z_{60} gives the best results. Contingency tables and verification scores for different wind speed thresholds at z_{30} confirm that MESO simulation gives slightly better results than LES (Figure 4). This is illustrated by the fact that the probability of detection (POD) is greater than the false alarm ratio (FAR) for a wider wind speed range in MESO than in LES simulations. The wind speed threshold at which POD is over FAR is around 5.5 m s^{-1} in MESO and 4.25 m s^{-1} in LES simulations. These wind speed thresholds increase in height for z_{45} and z_{60} although the difference between MESO and LES is maintained (not shown).

Threat scores (TS) are very similar between MESO and LES simulations, giving a comparable fraction of observed and forecasted events that were correctly predicted.

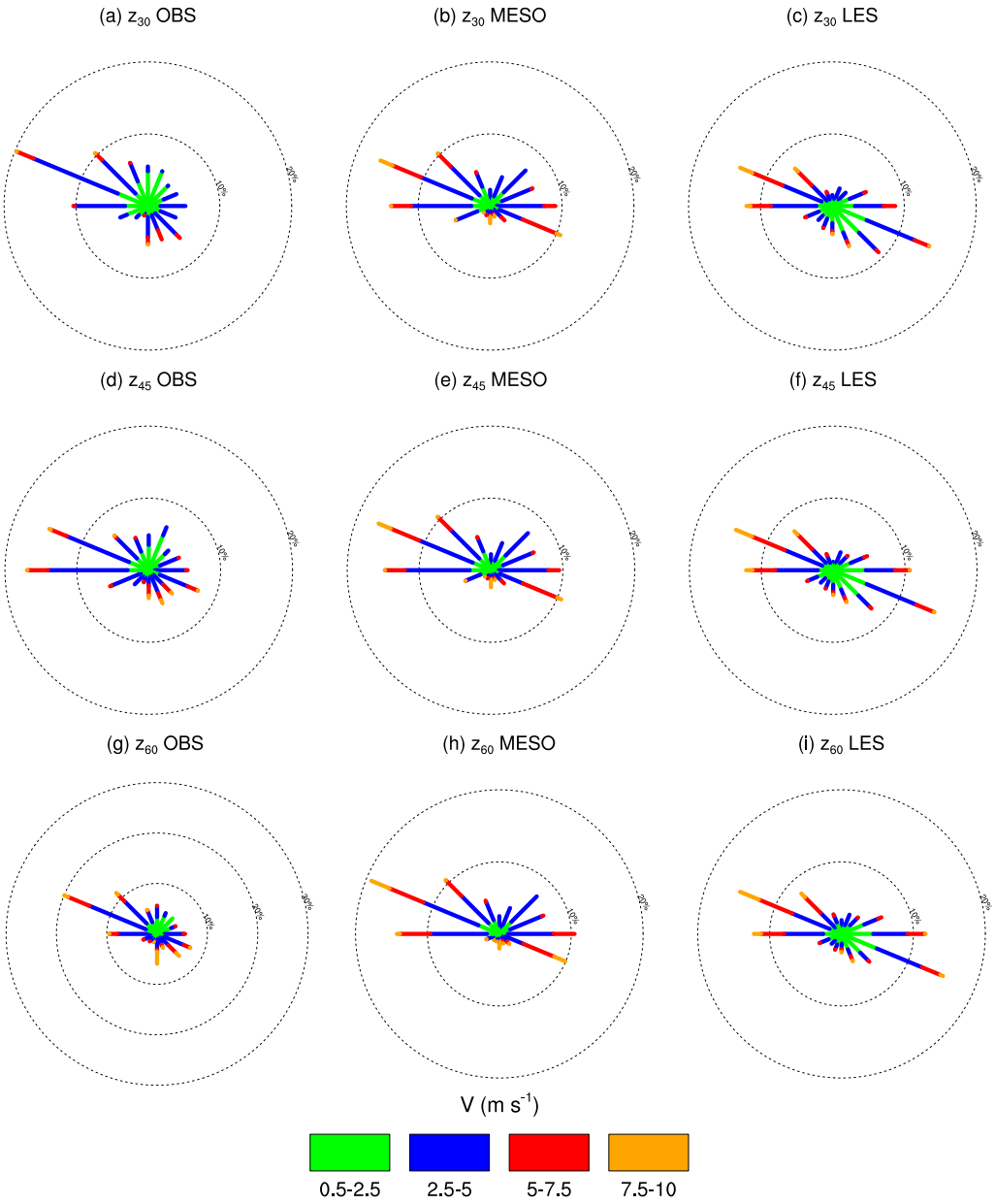

Figure 2. Wind roses with the wind distribution for the whole BLLAST period at three different heights. (**a**) Observations (OBS) at z_{30}. (**b**) WRF mesoscale 1-km resolution (MESO) at z_{30} m. (**c**) WRF-LES 111-m resolution (LES) at z_{30}. (**d**) OBS at z_{45}. (**e**) MESO at z_{45}. (**f**) LES at z_{45}. (**g**) OBS at z_{60}. (**h**) MESO at z_{60}. (**i**) LES at z_{60}.

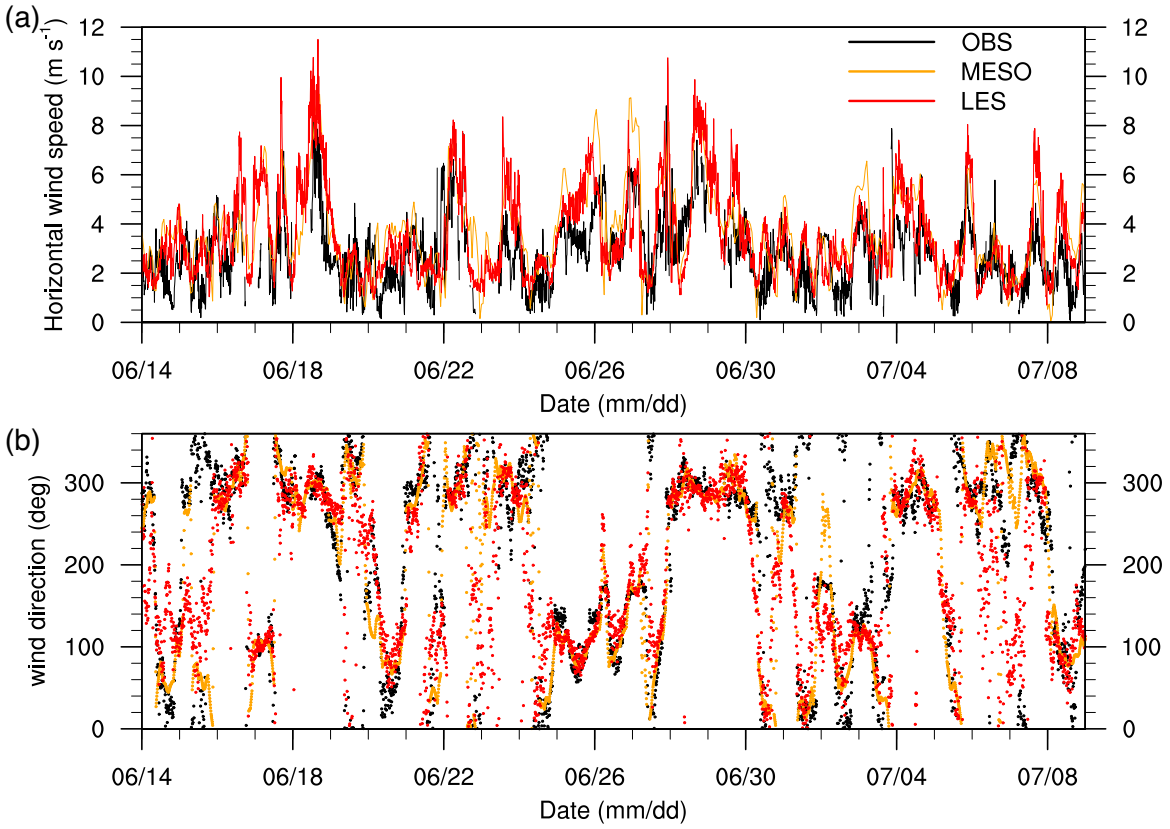

Figure 3. Time series of observed (OBS), mesoscale simulation of 1-km horizontal grid (MESO) and LES simulation of 111-m horizontal grid (LES) at z_{30}: (**a**) Horizontal wind speed. (**b**) Horizontal wind direction.

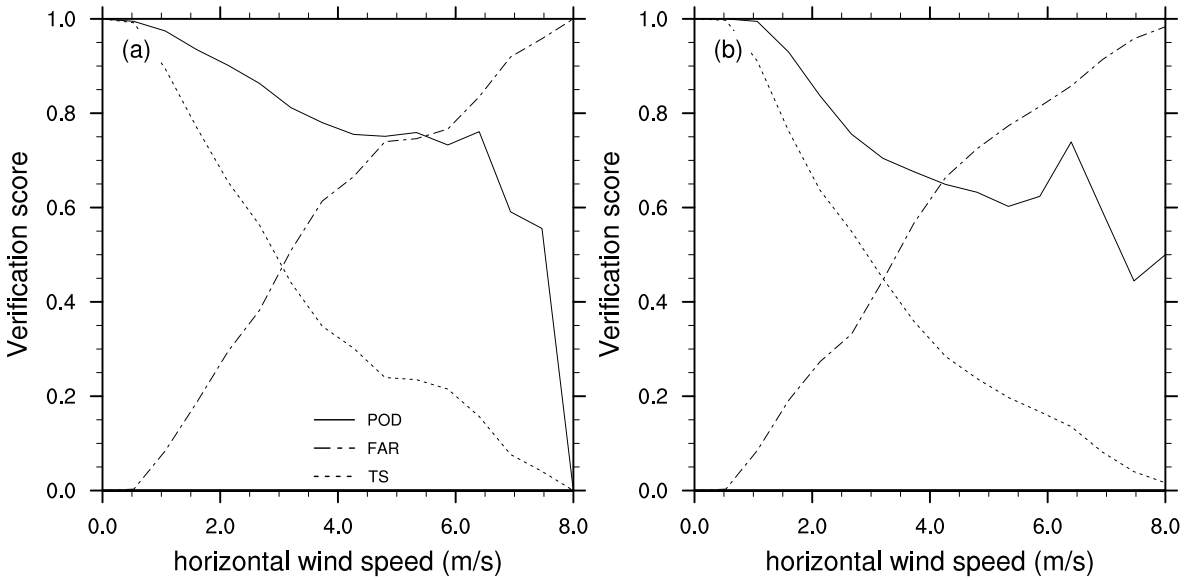

Figure 4. Verification scores for different horizontal wind speed thresholds including probability of detection (POD), false alarm ratio (FAR) and threat score (TS) for: (**a**) MESO simulation (**b**) LES simulation.

Table 3. Statistics for horizontal wind speed.

Level	z_{30}		z_{45}		z_{60}	
Statistic [units]	**MESO**	**LES**	**MESO**	**LES**	**MESO**	**LES**
MB [m s^{-1}]	0.92	0.64	0.43	0.29	0.54	0.09
RMSE [m s^{-1}]	1.35	1.25	1.10	1.27	1.45	1.52
R	0.52	0.45	0.61	0.46	0.66	0.58

The wind direction evolution time series plot shows that MESO and LES capture the main changes in wind direction, which were shown in the general statistics by the wind roses. In particular, simulations reproduce south-eastern dominant winds during the hot period (from 25 to 27 June) defined by [64] (Figure 3b) or the wind shift during intensive observation periods (IOP) days (19–20 June, 24–25 June, 1–2 July, 2–3 July) from north (daytime) to south (night-time) components. Statistics for wind direction show negative mean bias meaning that, in average, modelled wind direction is shifted counterclockwise, greater for LES than for MESO simulations, similar at all levels (Table 4). The square root of the average of squared errors shows a greater difference in LES modelled wind direction than in MESO in all levels, with magnitudes between 35 and 51 degrees. Therefore, MESO simulation, at three levels, performs slightly better the wind direction than LES. Linear regression coefficient for wind direction, calculated using directional statistics following [65,66], shows a very good regression between MESO and OBS (increasing from 0.86 at z_{30} to 0.96 at z_{60}). The R is slightly worse for LES.

Table 4. Statistics for wind direction.

Level	z_{30}		z_{45}		z_{60}	
Statistic [units]	**MESO**	**LES**	**MESO**	**LES**	**MESO**	**LES**
MB [deg]	−11.16	−16.24	−5.94	−9.65	−13.01	−16.60
RMSE [deg]	35.37	51.37	35.30	48.24	35.08	43.62
R	0.86	0.63	0.88	0.67	0.96	0.76

In general, the wind statistics show similar behaviour between MESO and LES simulations (Tables 3 and 4), slightly better for MESO, meaning that the mesoscale forcing, driven by the reanalysis forcing, is the responsible for the changes in wind speed and wind direction. The LES simulation does not improve the wind field, instead, it shows higher variability in wind speed and wind direction values. As the wind time series in LES are calculated using 10 min temporal averages from 0.25 s outputs, they include more fluctuations and variability than MESO time series, therefore, statistics can easily be worse for LES. In fact this could be somewhat expected due to the 'double penalty' effect [67,68], caused by miss-location (in this case temporal shifts) of forecast features found when comparing higher with lower resolution forecasts with deterministic verification scores. The added value of LES is, then, the ability to resolve turbulent quantities (see next Section 3.2).

3.2. Model Performance: Turbulent Quantities

One of the most important magnitudes in the ABL is the turbulent kinetic energy (TKE), which defines the status of the flow and the energy available in the atmosphere for mixing, i.e., the turbulence intensity. The temporal evolution of the TKE at z_{30} is shown in Figure 5. While in MESO simulation the TKE is obtained from the parametrisation of the PBL scheme, in LES this magnitude is explicitly calculated (see Section 2.3). For the whole period, the MESO and LES simulations reproduce the daily cycle of the TKE and reproduce the turbulence intensity changes through time. Although the correlation is very good at all levels (Table 5), MESO simulation, as expected, is not able to capture the observed turbulence peaks, while LES approximates better the enhanced TKE periods (18, 22, 28 June and 3 of July) but generally underestimating the turbulence

intensity. These days correspond to non-IOP periods, when large scale winds from W and N dominated the region.

An examination of the data distributions (probability distribution functions, or PDF) from the whole period LES simulation and observations allows a global comparison of the behaviours and discrepancies between the two data sets. For example, LES simulation generally underestimates TKE values (Figure 6a), either during night-time or during daytime, and extreme TKE values are not well captured. This is also shown by the negative MB at all levels (Table 5), while R coefficients are maintained around 0.45–0.49. The horizontal wind standard deviation ranges are underestimated (Figure 6b), but most significantly, the vertical velocity standard deviation (Figure 6c). While the model hardly reaches values of σ_w greater than 0.2 m s^{-1} (more than 90% of values are below 0.2 m s^{-1}), more than the 70% of observations range between 0.2 to 0.6 m s^{-1} (Figure 6c). Very low values of the kinematic heat flux (F_H) are captured by LES (Figure 6d). Positive peaks are often underestimated, corresponding to central hours daytime maxima during IOP days. Linear regression coefficient is relatively low, decreasing as the height increases (Table 5). These results are only displayed for z_{30}, although the other two heights (z_{45} and z_{60}) show very similar PDF distributions for observations and simulations. Statistics for these heights are shown in Table 5.

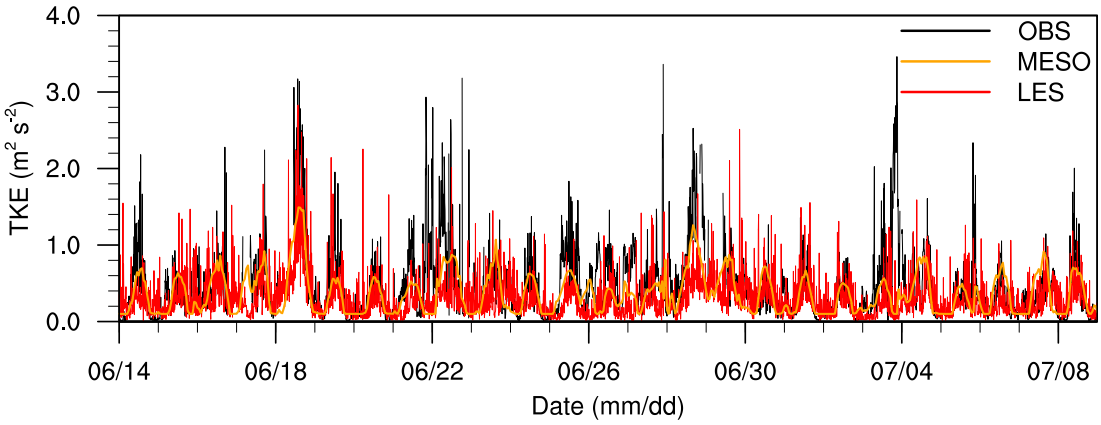

Figure 5. Time series of turbulent kinetic energy (TKE) from observations (OBS), mesoscale simulation of 1-km horizontal grid (MESO) and LES simulation of 111-m horizontal grid (LES) at z_{30}.

Table 5. Statistics for turbulent quantities. Note that the regression coefficient is dimensionless.

Magnitude [units]	**TKE [m^2 s^{-2}]**						**F_H [K m s^{-1}]**		
Level	**z_{30}**		**z_{45}**		**z_{60}**		**z_{30}**	**z_{45}**	**z_{60}**
	MESO	**LES**	**MESO**	**LES**	**MESO**	**LES**	**LES**	**LES**	**LES**
MB	−0.11	−0.16	−0.09	−0−17	−0.10	−0.15	0	0	−0.01
RMSE	0.24	0.33	0.24	0.32	0.25	0.33	0.03	0.04	0.05
R	0.97	0.45	0.91	0.49	0.93	0.48	0.39	0.17	0.15

A closer look to the daily cycle of the turbulent quantities confirms the general underestimation of TKE and heat flux values, calculated for 10 IOP days (Figure 7). The TKE daily cycle (Figure 7a) is generally underestimated by LES, a feature also observed by [12], but opposite to the results from [6]. These authors and other recent existing literature [22,35,37] use a greater number of vertical levels which can be one reason for these discrepancies. In addition, the sub-grid scheme may not be providing the fully correct energy contained in the eddies smaller than the grid, which can be another source of errors. While morning median and peaks are too low in the simulation, afternoon median gets closer to observations, which means that turbulence in the simulation probably needs more time to get fully developed. Night-time TKE values are maintained in the simulation, although slightly below the observed ones.

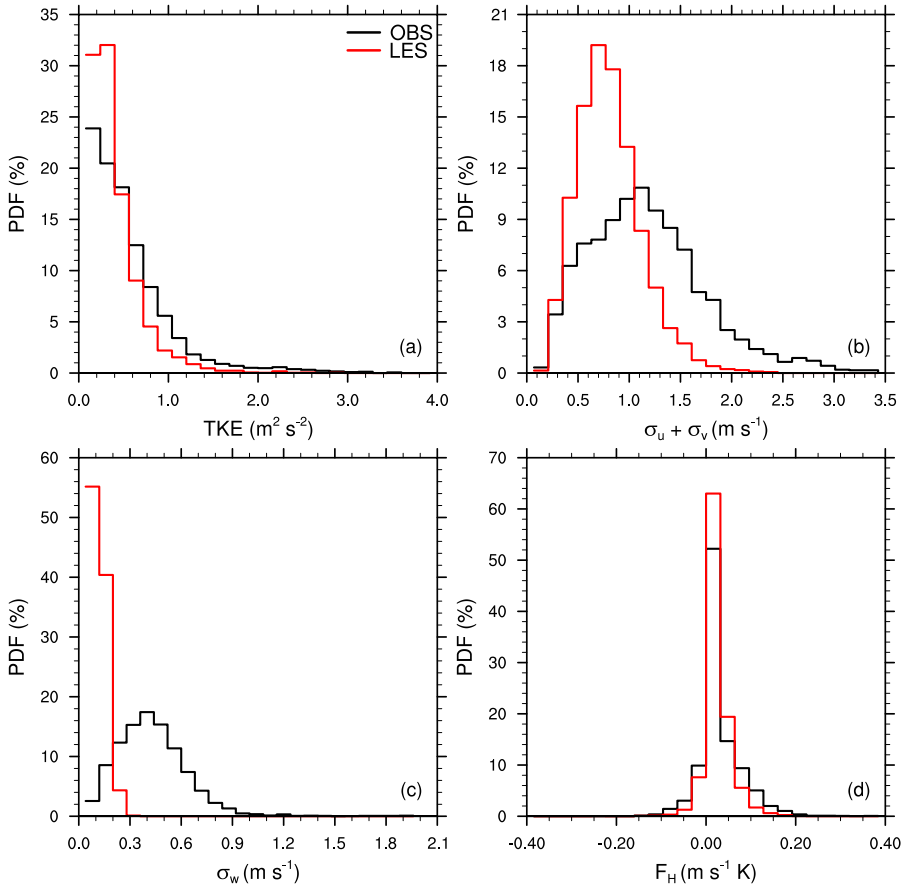

Figure 6. Probability distribution function (PDF) of observed (OBS) and LES simulation of 111-m horizontal grid (LES) at z_{30} of: (**a**) Turbulent kinetic energy (TKE). (**b**) Standard deviation of horizontal wind components ($\sigma_u + \sigma_v$). (**c**) Standard deviation of vertical velocity component (σ_w). (**d**) Kinematic heat flux (F_H).

The daily cycle seen in heat flux observations is misrepresented by the LES simulation (Figure 7b). During night-time the simulation maintains the heat flux close to zero, mostly positive, whereas in observations the median heat flux is negative, with values around -0.02 K m s^{-1}. During daytime the magnitude of F_H is noticeably underestimated, and extreme positive values are never reached, a similar behaviour than observed by [2]. Greater values of F_H are given by LES during IOP daytime central hours in comparison to non-IOP days. Therefore, transport due to thermal origin of turbulence is reproduced by LES to some degree. Instead, no remarkable differences are noticed in the comparison of TKE for the non-IOP days.

The general inaccuracy of the model in reproducing the heat flux can be attributed to different explanations. Firstly, we have seen there is a general underestimation of the standard deviation of vertical velocity component (Figure 6c), which can lead to an underestimation of the heat flux, and the TKE as well. In addition, a great part of the heat flux may be unresolved given the grid resolution. Thus, the sub-grid part of the heat flux becomes significant, which is not resolved by the simulation, as Figure 7b only presents the resolved heat flux. Indeed, in our 111-m horizontal grid size simulations eddies that trigger turbulence may be smaller than the effective resolution, for instance in stably stratified ABL (e.g., [36]). Then, the sub-grid scheme of the model can play an important role, as most part of the heat flux is unresolved and has to be parameterised and it still exists a lot of uncertainty to represent adequately the unresolved sub-grid turbulence. In addition, the grid geometry lead to high anisotropy, breaking the assumption of the LES simulation. On the other hand, the temperature perturbation method used to couple the mesoscale to LES domains can be introducing artificial unrealistic potential temperature fluctuations.

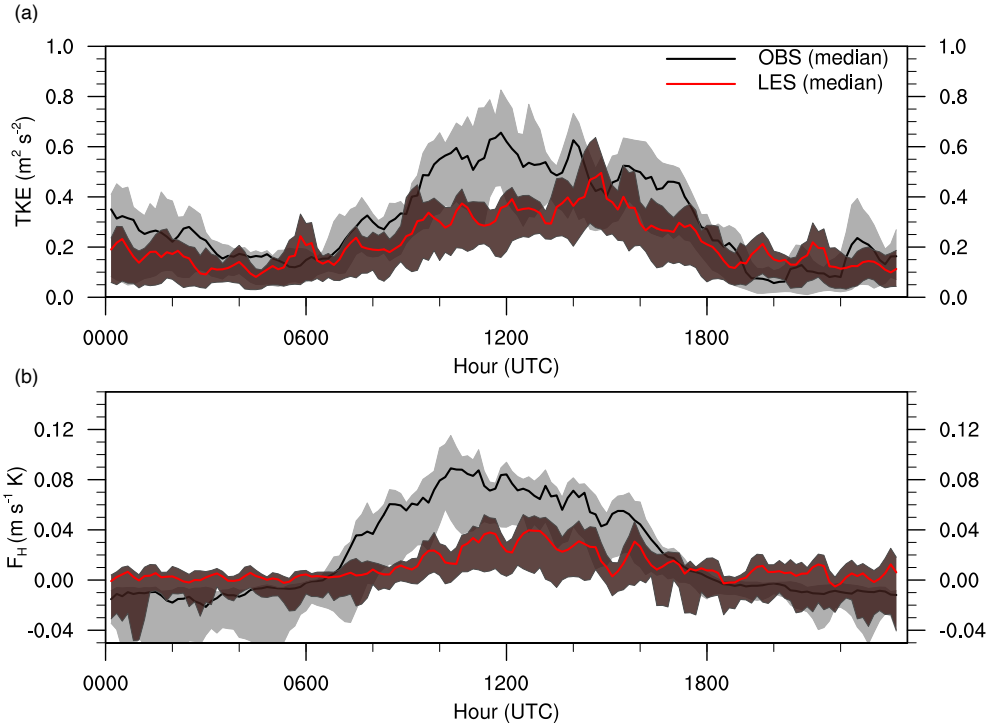

Figure 7. Daily cycle of observed (OBS) and LES simulation of 111-m horizontal grid (LES) at z_{30} for IOP days: (**a**) Turbulent kinetic energy (TKE). (**b**) Kinematic heat flux (F_H). Solid thick lines correspond to the median of OBS (black) and LES (red). Light grey shaded area corresponds to OBS data between percentile 25 and 75. Dark grey semitransparent shaded area corresponds to LES data between percentile 25 and 75. Data is smoothed every 30 min.

3.3. Velocity Field Spectrum

The power spectral density of the turbulent velocity field, or turbulence spectrum, gives information about the energy associated with each time scale. In this case we can explore the energy associated to limited time scales, between 25 days and 10 min. Figure 8 shows that the energy of eddies with lifetime below 2 or 3 h are maintained in LES simulation, similarly as in observed wind speed spectrum (OBS), but decays too fast in MESO simulation. Therefore, MESO simulation is not able to resolve sufficient energy for frequencies higher than 10^{-4} (i.e., lower than 2 h), producing a strong decay of the energy. Instead, LES is reproducing the eddies lifetime with similar energy than in observations. The lack of energy identified for frequencies of a few hours in LES can be attributed to the unresolved flow field in the "Terra incognita" scales, probably not fully resolved in the intermediate LES domain.

On the left part of the turbulence spectrum, the energy in the smallest range of frequencies (larger scales) is slightly overestimated in MESO an LES simulations, in comparison with OBS time series, a limitation probably dragged from the reanalysis. In addition, large scales, from several days to few hours are reproduced similarly in both MESO and LES simulations.

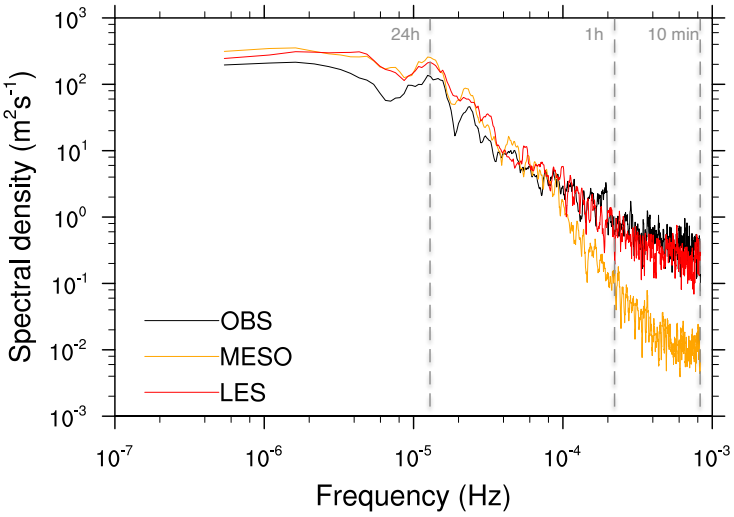

Figure 8. Turbulence spectrum of observed (OBS), mesoscale (MESO) and LES simulation of 111-m horizontal grid (LES) at z_{30}.

4. Conclusions

This study demonstrates the ability of the WRF-LES modelling system to simulate the mean and turbulent quantities of the flow field during the 25 days when BLLAST campaign took place. The long WRF-LES simulation and the field campaign observational data sets provide a unique opportunity to identify the benefits and shortcomings of the mesoscale (MESO) and LES simulations for such a long time period.

The large scale winds are well represented by simulations, and the enhanced turbulence associated with the strong winds as well. Mesoscale flows from north during daytime veering to south during night-time are quite well reproduced by both MESO and LES simulations. The general statistics for wind speed and direction are slightly better for MESO than for LES, although the differences are small and statistics can harm LES because of the greater fluctuations of the time series. Few differences in wind speed and wind direction are seen between levels, better for the highest level, z_{60}, to some degree.

The daily cycle of the turbulent kinetic energy (TKE) is reproduced by LES but values are generally underestimated, mostly during daytime morning and central hours. Non-IOP periods with enhanced turbulence are reproduced by the simulation, but still lowering the intensity. Although the horizontal wind standard deviations are lower in LES than in OBS, the simulation mostly fails in reproducing too low vertical velocity standard deviation. In addition, LES underestimates the daytime heat flux peaks and is not able to reproduce the mostly negative heat flux at night. As shown by [36], simulations at smaller grid sizes would probably resolve a larger part of turbulence, helping to better approximate the turbulent processes. However, there is still a lot of uncertainty in the role of the sub-grid scheme, when the unresolved scales are significant. Despite the test performed with a higher number of levels in the boundary layer indicated similar results, future work should be devoted to test further model configurations with different physical parametrisation schemes and higher number of levels.

In terms of the energy associated with the wind speed resolved in the different time scales, it is shown that LES is able to reproduce sufficient energy for all the turbulence spectrum frequencies, while MESO is limited to time scales larger than a few hours. For higher frequencies, MESO produces a too strong decay of energy where eddies of lifetime smaller than few hours are not reproduced. Therefore, as already documented in previous research, this study also confirms the ability of LES simulation to represent the small scale motions of lifetime around few minutes.

This work provides an insight in the use of high resolution numerical modelling using WRF-LES. WRF-MESO still provides slightly better results for horizontal wind speed and wind direction. The major shortcomings of WRF-LES seem to be related to the grid resolution, which establishes

the limit for the scale of resolved turbulence. Another key factor seems to be the underestimation of the unresolved turbulent quantities, given by the sub-grid scheme, that may be important at our LES grid size of 111-m. Further research would include testing for real simulations including sensitivity studies with different grid resolution, increasing vertical levels and exploring the role of the sub-grid scheme. In addition, as pointed out by [2], a fully 3D PBL turbulence parameterisation is probably needed to correctly resolve the flow field mean and turbulent quantities in intermediate domains in the range of the "Terra incognita" [69], to provide better inflow conditions for nested LES domains.

Author Contributions: Conceptualisation, M.U., À.M., P.C. and J.B.; methodology, M.U., À.M. and P.C.; software, À.M. and P.C.; validation, M.U.; formal analysis, M.U.; investigation, M.U., À.M., P.C., J.B. and B.K. ; resources, M.U., À.M., P.C. and J.B.; data curation, M.U., À.M. and P.C.; writing—original draft preparation, M.U.; writing—review and editing, M.U., À.M., P.C., J.B. and B.K.; visualisation, M.U.; supervision, M.U., À.M., P.C., J.B. and B.K.; project administration, J.B.; funding acquisition, J.B. All authors have read and agreed to the published version of the manuscript.

Funding: This research was funded by the Spanish projects CGL2015-65627-C3-2-R (MINECO/FEDER), CGL2016-81828-REDT (AEI) and RTI2018-098693-B643-C32 (AEI).

Acknowledgments: The BLLAST field experiment was made possible thanks to the contribution of several institutions and supports: INSU-CNRS (Institut National des Sciences de l'Univers, Centre national de la Recherche Scientifique, LEFE-IDAO program), Météo-France, Observatoire Midi-Pyrénées (University of Toulouse), EUFAR (EUropean Facility for Airborne Research) and COST ES0802 (European Cooperation in the field of Scientific and Technical). The field experiment would not have occurred without the contribution of all participating European and American research groups, which all have contributed in a significant amount (see supports). BLLAST field experiment was hosted by the instrumented site of Centre de Recherches Atmosphériques, Lannemezan, France (Observatoire Midi-Pyrénées, Laboratoire d'Aérologie). Its 60 m (["Valimev"]) tower was partly supported by the POCTEFA/FLUXPYR European program. BLLAST data are managed by SEDOO, from the Observatoire Midi-Pyrénées. As well as for the responsibles of the instruments and data that we have used: Fabienne Lohou, PI of surface measurements in BLLAST, Frédérique Saïd, Solène Derrien for the 60 m instrumentation and data, Eric Pardyjak and Daniel Alexander for the 8 m ("Skinflow") tower. Also to the P2OA instrumented site, since the Centre de Recherches Atmosphériques of Lannemezan is part of an instrumented platform called Pyrenean Platform of the Observation of the Atmosphere (http://p2oa.aero.obs-mip.fr). P2OA facilities and staff are funded and supported by the Observatoire Midi-Midi-Pyrénées (University of Toulouse, France) and CNRS (Centre National de la Recherche Scientifique). We acknowledge Marie Lothon for her helpful suggestions and Fabienne Lohou, for providing the data of the Valimev Tower.

Conflicts of Interest: The authors declare no conflict of interest.

Appendix A. WRF-LES Simulation Using Enhanced Vertical Resolution

A 4-day long simulation increasing the number of vertical levels is run, covering the period from 1 to 4 July 2011. Vertical levels are increased from 15 to 22 in the first km of atmosphere, that is a similar number of levels used in some recent existing literature with WRF-LES [35,37] but still fewer than other very recent studies [6,22], all of them simulating short periods of time, including one or few days.

Results show similar tendencies and daily variations between simulations. Similar metrics for wind speed, wind direction and heat flux are obtained (not shown). The enhanced vertical level simulation (LES_2) reveals a smoother behaviour of the TKE, giving a better regression coefficient (R_LES =0.23; R_LES_2= 0.63), mainly because fluctuations diminish, as shown in the example of Figure A1. However, MB (MB_LES $= -0.15$ m^2 s^{-2}; MB_LES_2 $= -0.33$ m^2 s^{-2}) and RMSE (RMSE_LES $= 0.31$ m^2 s^{-2}; RMSE_LES_2 $= 0.34$ m^2 s^{-2}) are barely improved in the new configuration.

Figure A2 shows the probability distribution functions for the 4-day simulated period comparing simulations. Similar data distributions between simulations are observed. TKE is too low in the increased level simulation, maybe due to the subgrid scale (SGS) model which may not be representing enough energy of the eddies smaller than the grid size.

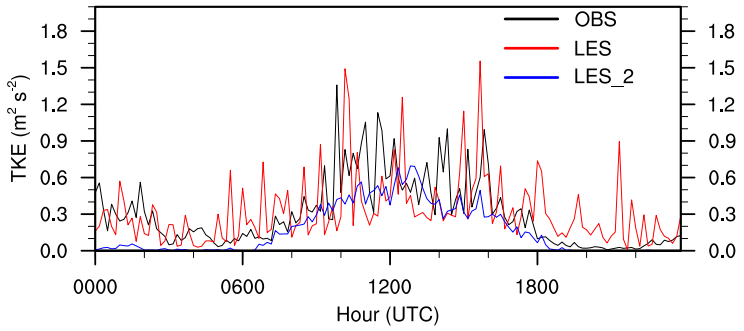

Figure A1. Turbulent kinetic energy (TKE) evolution for 1 July 2011 comparing observed (OBS), original LES simulation (LES) and LES simulation with enhanced vertical levels (LES_2) at z_{30}.

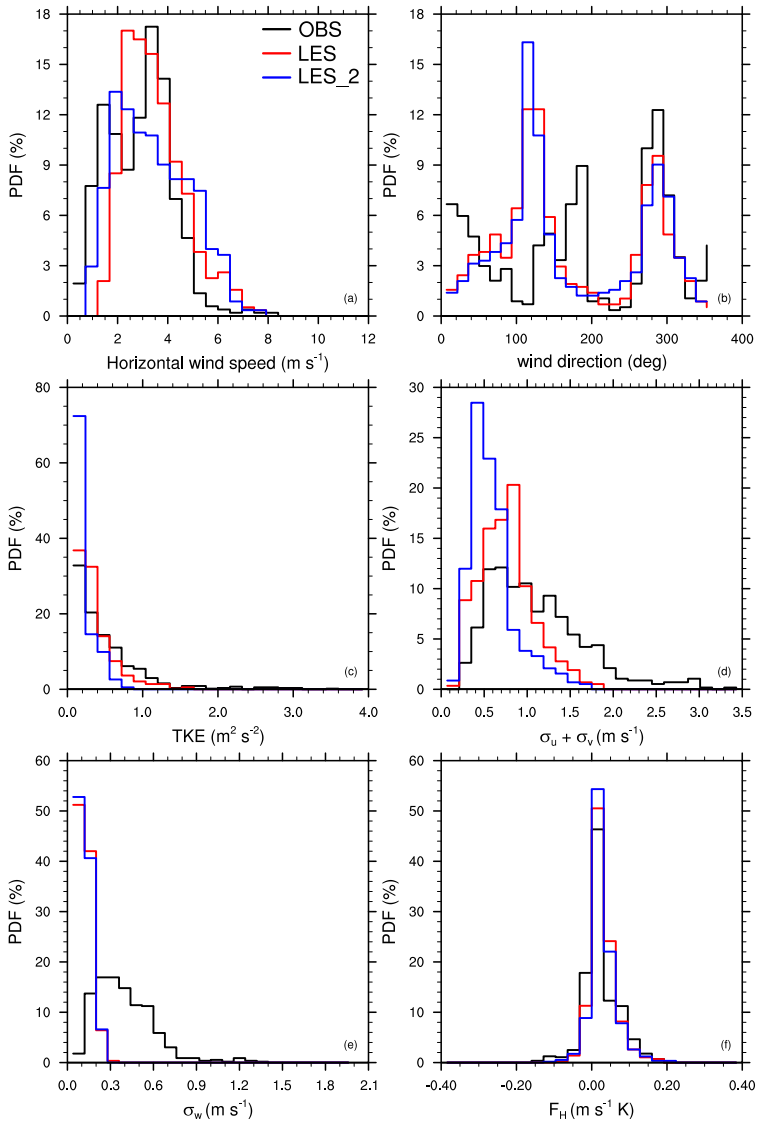

Figure A2. Probability distribution function (PDF) of observed (OBS), original LES simulation (LES) and LES simulation with enhanced vertical levels (LES_2) at z_{30} of: (**a**) Horizontal wind speed. (**b**) Wind direction. (**c**) Turbulent kinetic energy (TKE). (**d**) Standard deviation of horizontal wind components ($\sigma_u + \sigma_v$). (**e**) Standard deviation of vertical velocity component (σ_w). (**f**) Kinematic heat flux (F_H).

Appendix B. Contingency Tables

Following Contingency tables are used to evaluate the forecast of horizontal wind speed exceeding specific thresholds, based on the classification of Table A1.

Table A1. Contingency table.

		Observed		
		Yes	No	
Simulated	Yes	a	b	a+b
	No	c	d	c + d
		a + c	b + d	n = a + b + c + d

Following [70,71], indexes of threat score (TS), probability of detection (POD) and false alarm ratio (FAR) are calculated using letters indicated in Table A1, as follows:

$$TS = \frac{a}{a+b+c} \tag{A1}$$

$$POD = \frac{a}{a+c} \tag{A2}$$

$$FAR = \frac{b}{a+b} \tag{A3}$$

where a perfect score is given by TS = 1, POD = 1 and FAR = 0.

References

1. Powers, J.G.; Klemp, J.B.; Skamarock, W.C.; Davis, C.A.; Dudhia, J.; Gill, D.O.; Coen, J.L.; Gochis, D.J.; Ahmadov, R.; Peckham, S.E.; et al. The weather research and forecasting model: Overview, system efforts, and future directions. *Bull. Am. Meteorol. Soc.* **2017**, *98*, 1717–1737. [CrossRef]
2. Kosović, B.; Munoz, P.J.; Juliano, T.; Martilli, A.; Eghdami, M.; Barros, A.; Haupt, S. Three-Dimensional Planetary Boundary Layer Parameterization for High-Resolution Mesoscale Simulations. *J. Phys. Conf. Ser.* **2020**, *1452*, 012080. [CrossRef]
3. Moeng, C.; Dudhia, J.; Klemp, J.; Sullivan, P. Examining two-way grid nesting for large eddy simulation of the PBL using the WRF model. *Mon. Weather Rev.* **2007**, *135*, 2295–2311. [CrossRef]
4. Wyngaard, J.C. Toward numerical modeling in the "Terra Incognita". *J. Atmos. Sci.* **2004**, *61*, 1816–1826. [CrossRef]
5. Chow, F.K.; Schär, C.; Ban, N.; Lundquist, K.A.; Schlemmer, L.; Shi, X. Crossing multiple gray zones in the transition from mesoscale to microscale simulation over complex terrain. *Atmosphere* **2019**, *10*, 274. [CrossRef]
6. Doubrawa, P.; Muñoz-Esparza, D. Simulating Real Atmospheric Boundary Layers at Gray-Zone Resolutions: How Do Currently Available Turbulence Parameterizations Perform? *Atmosphere* **2020**, *11*, 345. [CrossRef]
7. Haupt, S.E.; Kosovic, B.; Shaw, W.; Berg, L.K.; Churchfield, M.; Cline, J.; Draxl, C.; Ennis, B.; Koo, E.; Kotamarthi, R.; et al. On Bridging A Modeling Scale Gap: Mesoscale to Microscale Coupling for Wind Energy. *Bull. Am. Meteorol. Soc.* **2020**, *100*, 2533–2550. [CrossRef]
8. Letzel, M.O.; Krane, M.; Raasch, S. High resolution urban large-eddy simulation studies from street canyon to neighbourhood scale. *Atmos. Environ.* **2008**, *42*, 8770–8784. [CrossRef]
9. Kurppa, M.; Hellsten, A.; Auvinen, M.; Raasch, S.; Vesala, T.; Järvi, L. Ventilation and air Quality in city blocks using large-eddy simulation—urban planning perspective. *Atmosphere* **2018**, *9*, 65. [CrossRef]
10. Chatzimichailidis, A.E.; Argyropoulos, C.D.; Assael, M.J.; Kakosimos, K.E. Qualitative and quantitative investigation of multiple large eddy simulation aspects for pollutant dispersion in street canyons using OpenFOAM. *Atmosphere* **2019**, *10*, 17. [CrossRef]
11. Wu, Y.T.; Porté-Agel, F. Large-eddy simulation of wind-turbine wakes: Evaluation of turbine parametrisations. *Bound. Layer Meteorol.* **2011**, *138*, 345–366. [CrossRef]

12. Doubrawa, P.; Montornès, A.; Barthelmie, R.J.; Pryor, S.C.; Giroux, G.; Casso, P. Effect of Wind Turbine Wakes on the Performance of a Real Case WRF-LES Simulation. *J. Phys. Conf. Ser.* **2017**, *854*, 012010. [CrossRef]
13. Abkar, M. Impact of subgrid-scale modeling in actuator-line based large-eddy simulation of vertical-axis wind turbine wakes. *Atmosphere* **2018**, *9*, 257. [CrossRef]
14. McGrattan, K.B.; Baum, H.R.; Rehm, R.G. Numerical simulation of smoke plumes from large oil fires. *Atmos. Environ.* **1996**, *30*, 4125–4136. [CrossRef]
15. Moisseeva, N.; Stull, R. Capturing Plume Rise and Dispersion with a Coupled Large-Eddy Simulation: Case Study of a Prescribed Burn. *Atmosphere* **2019**, *10*, 579. [CrossRef]
16. Khairoutdinov, M.; Kogan, Y. A new cloud physics parameterization in a large-eddy simulation model of marine stratocumulus. *Mon. Weather Rev.* **2000**, *128*, 229–243. [CrossRef]
17. Neves, T.; Fisch, G.; Raasch, S. Local convection and turbulence in the Amazonia using large eddy simulation model. *Atmosphere* **2018**, *9*, 399. [CrossRef]
18. Brune, S.; Kapp, F.; Friederichs, P. A wavelet-based analysis of convective organization in ICON large-eddy simulations. *Q. J. R. Meteorol. Soc.* **2018**, *144*, 2812–2829. [CrossRef]
19. Flossmann, A.I.; Wobrock, W. Cloud Processing of Aerosol Particles in Marine Stratocumulus Clouds. *Atmosphere* **2019**, *10*, 520. [CrossRef]
20. Stevens, B.; Lenschow, D.H. Observations, experiments, and large eddy simulation. *Bull. Am. Meteorol. Soc.* **2001**, *82*, 283–294. [CrossRef]
21. Cuxart, J. When can a high-resolution simulation over complex terrain be called LES? *Front. Earth Sci.* **2015**, *3*, 87. [CrossRef]
22. Liu, Y.; Liu, Y.; Muñoz-Esparza, D.; Hu, F.; Yan, C.; Miao, S. Simulation of Flow Fields in Complex Terrain with WRF-LES: Sensitivity Assessment of Different PBL Treatments. *J. Appl. Meteorol. Climatol.* **2020**, *59*, 1481–1501. [CrossRef]
23. Lehner, M.; Whiteman, C.D.; Hoch, S.W.; Crosman, E.T.; Jeglum, M.E.; Cherukuru, N.W.; Calhoun, R.; Adler, B.; Kalthoff, N.; Rotunno, R.; et al. The METCRAX II field experiment: A study of downslope windstorm-type flows in Arizona's Meteor Crater. *Bull. Am. Meteorol. Soc.* **2016**, *97*, 217–235. [CrossRef]
24. Udina, M.; Soler, M.R.; Sol, O. A Modeling Study of a Trapped Lee-Wave Event over the Pyrénées. *Mon. Weather Rev.* **2017**, *145*, 75–96. [CrossRef]
25. Udina, M.; Bech, J.; Gonzalez, S.; Soler, M.R.; Paci, A.; Miró, J.R.; Trapero, L.; Donier, J.M.; Douffet, T.; Codina, B.; et al. Multi-sensor observations of an elevated rotor during a mountain wave event in the Eastern Pyrenees. *Atmos. Res.* **2020**, *234*, 104698. [CrossRef]
26. Caccamo, M.; Castorina, G.; Colombo, F.; Insinga, V.; Maiorana, E.; Magazù, S. Weather forecast performances for complex orographic areas: Impact of different grid resolutions and of geographic data on heavy rainfall event simulations in Sicily. *Atmos. Res.* **2017**, *198*, 22–33. [CrossRef]
27. Yáñez-Morroni, G.; Gironás, J.; Caneo, M.; Delgado, R.; Garreaud, R. Using the weather research and forecasting (WRF) model for precipitation forecasting in an Andean region with complex topography. *Atmosphere* **2018**, *9*, 304. [CrossRef]
28. Gonzalez, S.; Bech, J.; Udina, M.; Codina, B.; Paci, A.; Trapero, L. Decoupling between Precipitation Processes and Mountain Wave Induced Circulations Observed with a Vertically Pointing K-Band Doppler Radar. *Remote Sens.* **2019**, *11*, 1034. [CrossRef]
29. Castorina, G.; Caccamo, M.T.; Magazù, S. Study of convective motions and analysis of the impact of physical parametrization on the WRF-ARW forecast model. *Atti Della Accad. Peloritana Pericolanti Cl. Sci. Fis. Mat. E Nat.* **2019**, *97*, 19.
30. Wagner, J.; Gerz, T.; Wildmann, N.; Gramitzky, K. Long-term simulation of the boundary layer flow over the double-ridge site during the Perdigão 2017 field campaign. *Atmos. Chem. Phys.* **2019**, *19*, 1129–1146. [CrossRef]
31. Xue, H.; Li, J.; Qian, T.; Gu, H. A 100-m-Scale Modeling Study of a Gale Event on the Lee Side of a Long Narrow Mountain. *J. Appl. Meteorol. Climatol.* **2020**, *59*, 23–45. [CrossRef]
32. Muñoz-Esparza, D.; Kosović, B.; García-Sánchez, C.; van Beeck, J. Nesting Turbulence in an Offshore Convective Boundary Layer Using Large-Eddy Simulations. *Bound. Layer Meteorol.* **2014**, *151*, 453–478. [CrossRef]

33. Udina, M.; Sun, J.; Kosović, B.; Soler, M.R. Exploring Vertical Turbulence Structure in Neutrally and Stably Stratified Flows Using the Weather Research and Forecasting–Large-Eddy Simulation (WRF–LES) Model. *Bound. Layer Meteorol.* **2016**, *161*, 355–374. [CrossRef]
34. El Guernaoui, O.; Reuder, J.; Esau, I.; Wolf, T.; Maronga, B. Scaling the decay of turbulence kinetic energy in the free-convective boundary layer. *Bound. Layer Meteorol.* **2019**, *173*, 79–97. [CrossRef]
35. Simon, J.S.; Zhou, B.; Mirocha, J.D.; Chow, F.K. Explicit filtering and reconstruction to reduce grid dependence in convective boundary layer simulations using WRF-LES. *Mon. Weather Rev.* **2019**, *147*, 1805–1821. [CrossRef]
36. Muñoz-Esparza, D.; Lundquist, J.K.; Sauer, J.A.; Kosović, B.; Linn, R.R. Coupled mesoscale-LES modeling of a diurnal cycle during the CWEX-13 field campaign: From weather to boundary-layer eddies. *J. Adv. Model. Earth Syst.* **2017**, *9*, 1572–1594. [CrossRef]
37. Cui, C.; Bao, Y.; Yuan, C.; Li, Z.; Zong, C. Comparison of the performances between the WRF and WRF-LES models in radiation fog–A case study. *Atmos. Res.* **2019**, *226*, 76–86. [CrossRef]
38. Lothon, M.; Lohou, F.; Pino, D.; Couvreux, F.; Pardyjak, E.; Reuder, J.; Vilà-Guerau de Arellano, J.; Durand, P.; Hartogensis, O.; Legain, D.; et al. The BLLAST field experiment: Boundary-Layer Late Afternoon and Sunset Turbulence. *Atmos. Chem. Phys. Discuss.* **2014**, *14*, 10789–10852. [CrossRef]
39. Trapero, L.; Bech, J.; Lorente, J. Numerical modelling of heavy precipitation events over Eastern Pyrenees: Analysis of orographic effects. *Atmos. Res.* **2013**, *123*, 368–383. [CrossRef]
40. Trapero, L.; Bech, J.; Duffourg, F.; Esteban Vea, P.; Lorente, J. Mesoscale numerical analysis of the historical November 1982 heavy precipitation event over Andorra (Eastern Pyrenees). *Nat. Hazards Earth Syst. Sci.* **2013**, *13*, 2969-2990 [CrossRef]
41. Lee, K.O.; Flamant, C.; Ducrocq, V.; Duffourg, F.; Fourrié, N.; Delanoë, J.; Bech, J. Initiation and development of a mesoscale convective system in the Ebro River Valley and related heavy precipitation over northeastern Spain during HyMeX IOP 15a. *Q. J. R. Meteorol. Soc.* **2017**, *143*, 942–956. [CrossRef]
42. Gonzalez, S.; Callado, A.; Werner, E.; Escribà, P.; Bech, J. Coastally trapped disturbances caused by the tramontane wind on the northwestern Mediterranean: Numerical study and sensitivity to short-wave radiation. *Q. J. R. Meteorol. Soc.* **2018**, *144*, 1321–1336. [CrossRef]
43. Said, F.; Derrien, S.; Pique, E.; Abadie, M.; Meyerfeld, Y.; Jarnot, C.; Martin, J.; Bezombes, Y.; Lohou, F.; Lothon, M.; et al. *POCTEFA/FluxPyr and BLLAST Campistrous Mast June and July 2011*. Available online: http://bllast.sedoo.fr/ (accessed on 2 September 2020).
44. Skamarock, W.C.; Klemp, J.; Dudhia, J.; Gill, D.; Barker, D.; Wang, W.; Powers, J. *A Description of the Advanced Research WRF Version 3*; NCAR Tech Notes-475+ STR; National Center for Atmospheric Research (NCAR): Boulder, CO, USA, 2008.
45. Vortex. Vortex-LES White Paper. Available online: https://vortexfdc.com/knowledge/vortex-les-white-paper/ (accessed on 2 September 2020).
46. Smagorinsky, J. General circulation experiments with the primitive equations. *Mon. Weather Rev.* **1963**, *91*, 99–164. [CrossRef]
47. Lilly, D.K. The representation of small scale turbulence in numerical simulation experiments. *Proc. Ibm Sci. Comput. Symp. Environ. Sci.* **1967**, *320–1951*, 195–210.
48. Muñoz-Esparza, D.; Kosović, B.; Mirocha, J.; van Beeck, J. Bridging the transition from mesoscale to microscale turbulence in numerical weather prediction models. *Bound. Layer Meteorol.* **2014**, *153*, 409–440. [CrossRef]
49. Muñoz-Esparza, D.; Kosović, B.; Van Beeck, J.; Mirocha, J. A stochastic perturbation method to generate inflow turbulence in large-eddy simulation models: Application to neutrally stratified atmospheric boundary layers. *Phys. Fluids* **2015**, *27*, 035102. [CrossRef]
50. Mlawer, E.J.; Taubman, S.J.; Brown, P.D.; Iacono, M.J.; Clough, S.A. Radiative transfer for inhomogeneous atmospheres: RRTM, a validated correlated-k model for the longwave. *J. Geophys. Res.* **1997**, *102*, 16663–16616. [CrossRef]
51. Dudhia, J. Numerical study of convection observed during the winter monsoon experiment using a mesoscale two-dimensional model. *J. Atmos. Sci.* **1989**, *46*, 3077–3107. [CrossRef]
52. Chen, F.; Dudhia, J. Coupling an advanced land surface-hydrology model with the Penn State-NCAR MM5 modeling system. Part I: Model implementation and sensitivity. *Mon. Weather Rev.* **2001**, *129*, 569–585. [CrossRef]

53. Jiménez, P.A.; Dudhia, J.; González-Rouco, J.F.; Navarro, J.; Montávez, J.P.; García-Bustamante, E. A revised scheme for the WRF surface layer formulation. *Mon. Weather Rev.* **2012**, *140*, 898–918. [CrossRef]
54. Janjić, Z.I. Nonsingular implementation of the Mellor–Yamada level 2.5 scheme in the NCEP Meso model. *NCEP Off. Note* **2002**, *437*, 61.
55. Hong, S.Y.; Dudhia, J.; Chen, S.H. A revised approach to ice microphysical processes for the bulk parameterization of clouds and precipitation. *Mon. Weather Rev.* **2004**, *132*, 103–120. [CrossRef]
56. Zhang, D.; Anthes, R.A. A high-resolution model of the planetary boundary layer- Sensitivity tests and comparisons with SESAME-79 data. *J. Appl. Meteorol.* **1982**, *21*, 1594–1609. [CrossRef]
57. Farr, T.G.; Rosen, P.A.; Caro, E.; Crippen, R.; Duren, R.; Hensley, S.; Kobrick, M.; Paller, M.; Rodriguez, E.; Roth, L.; et al. The shuttle radar topography mission. *Rev. Geophys.* **2007**, *45*, RG2004. [CrossRef]
58. Bontemps, S.; Defourny, P.; Van Bogaert, E.; Arino, O.; Kalogirou, V.; Perez, J.R. GLOBCOVER 2009-Products Description and Validation Report. 2011. Available online: https://epic.awi.de/id/eprint/31014/16/GLOBCOVER2009_Validation_Report_2-2.pdf (accessed on 2 September 2020).
59. Copernicus Climate Change Service (C3S): ERA5: Fifth Generation of ECMWF Atmospheric Reanalyses of the Global Climate. Copernicus Climate Change Service Climate Data Store (CDS). 2017. Available online: https://cds.climate.copernicus.eu/ (accessed on 30 May 2020).
60. Burns, S.; Horst, T.; Jacobsen, L.; Blanken, P.; Monson, R. Using sonic anemometer temperature to measure sensible heat flux in strong winds. *Atmos. Meas. Tech.* **2012**, *5*, 2095. [CrossRef]
61. Jiménez, M.A.; Cuxart, J.; Martínez-Villagrasa, D. Influence of a valley exit jet on the nocturnal atmospheric boundary layer at the foothills of the Pyrenees. *Q. J. R. Meteorol. Soc.* **2019**, *145*, 356–375. [CrossRef]
62. Yus-Díez, J.; Udina, M.; Soler, M.R.; Lothon, M.; Nilsson, E.; Bech, J.; Sun, J. Nocturnal boundary layer turbulence regimes analysis during the BLLAST campaign. *Atmos. Chem. Phys.* **2019**, *19*, 9495–9514. [CrossRef]
63. Román-Cascón, C.; Yagüe, C.; Arrillaga, J.; Lothon, M.; Pardyjak, E.; Lohou, F.; Inclán, R.; Sastre, M.; Maqueda, G.; Derrien, S.; et al. Comparing mountain breezes and their impacts on CO2 mixing ratios at three contrasting areas. *Atmos. Res.* **2019**, *221*, 111–126. [CrossRef]
64. Couvreux, F.; Bazile, E.; Canut, G.; Lothon, M.; Lohou, F.; Guichard, F.; Nilsson, E. Boundary-layer turbulent processes and mesoscale variability represented by Numerical Weather Prediction models during the BLLAST campaign. *Atmos. Chem. Phys. Discuss.* **2016**, *16*, 8983–9002. [CrossRef]
65. Bowers, J.; Morton, I.; Mould, G. Directional statistics of the wind and waves. *Appl. Ocean Res.* **2000**, *22*, 13–30. [CrossRef]
66. Mardia, K.V.; Jupp, P.E. *Directional Statistics*; John Wiley & Sons: New York, NY, USA, 2009.
67. Nurmi, P. *Recommendations on the Verification of Local Weather Forecasts*; ECMWF Technical Memorandum 430: Reading, UK, 2003; p. 19. [CrossRef]
68. Ebert, E.E. Fuzzy verification of high-resolution gridded forecasts: A review and proposed framework. *Meteorol. Appl. A J. Forecast. Pract. Appl. Train. Tech. Model.* **2008**, *15*, 51–64. [CrossRef]
69. Stoll, R.; Gibbs, J.A.; Salesky, S.T.; Anderson, W.; Calaf, M. Large-Eddy Simulation of the Atmospheric Boundary Layer. *Bound. Layer Meteorol.* **2020**. [CrossRef]
70. Wilks, D.S. *Statistical Methods in the Atmospheric Sciences*; Academic Press: San Diego, CA, USA, 2011.
71. Forecast Verification Methods Across Time and Space Scales. 2015. Available online: https://www.cawcr.gov.au/projects/verification/ (accessed on 2 September 2020).